REPORT DOCUMENTATION PAGE

Form Approved
OMB NO. 0704-0188

1. AGENCY USE ONLY (Leave Blank)	2. REPORT DATE April 26, 2005	3. REPORT TYPE AND DATES COVERED Final: 01 Mar 03 - 31 Jan 05

4. TITLE AND SUBTITLE
Synthesis of Bulk Nanostructured Al Alloys with Ultra-high Strength and Wear Resistance for Army Applications

5. FUNDING NUMBERS

DAA D19-03-1-0020

6. AUTHOR(S)
E.J. Lavernia

7. PERFORMING ORGANIZATION NAME(S) AND ADDRESS(ES)
University of California, Davis
One shields Ave
Davis, CA 95616

8. PERFORMING ORGANIZATION REPORT NUMBER

9. SPONSORING / MONITORING AGENCY NAME(S) AND ADDRESS(ES)

U. S. Army Research Office
P.O. Box 12211
Research Triangle Park, NC 27709-2211

10. SPONSORING / MONITORING AGENCY REPORT NUMBER

44431.9-MS

11. SUPPLEMENTARY NOTES
The views, opinions and/or findings contained in this report are those of the author(s) and should not be construed as an official Department of the Army position, policy or decision, unless so designated by other documentation.

12 a. DISTRIBUTION / AVAILABILITY STATEMENT

Approved for public release; distribution unlimited.

12 b. DISTRIBUTION CODE

13. ABSTRACT (Maximum 200 words)

Synthesis/processing of nanostructured (amorphous or ultra fine grained) materials was studied via various processing routes such as gas atomization, melt spinning, cryomilling, equal-channel angular pressing (ECAP) and conventional consolidation. Microstructures and mechanical properties of both the amorphous powders and consolidated bulk materials were characterized. The amorphous alloy of $Al_{85}Ni_{10}La_5$ (at.%) was fabricated in terms of melt-spun ribbons and particularly, gas-atomized powders (<25 μm). The kinetics and microstructure evolution during the devitrification process were carefully investigated using DSC, XRD, SEM, TEM, and SAXS. It was found that quenched-in fcc-Al nuclei present in amorphous $Al_{85}Ni_{10}La_5$ powders. Annealing at 235°C leads to growth of the quenched-in nuclei with the grain size stabilized around 10 nm. With increasing annealing temperatures (i.e., at 245 °C, 250 °C and 263 °C), the devitrification takes place via eutectic crystallization with a resultant grain size around 20 nm. At the temperatures >283°C, the devitrification tends to complete in a short time (~5 min), however, this alloy shows excellent thermal stability to resist grain growth. The influence of devitrification, under various annealing temperatures, on mechanical response was studied by nanoindentation technique.

Bulk nanostructured materials were synthesized by consolidating the amorphous $Al_{85}Ni_{10}La_5$ alloy powder with 5083 Al alloy powder milled under cryogenic temperature (cryomilling). The addition of cryomilled 5083 Al alloy is to further increase the specific strength for the bulk materials (e.g., >1000 MPa in compression with the density ~2.9 g/cc). The bulk nanostructured material also shows high strength at elevated temperatures (i.e., 400 MPa in compression at 200°C). At room temperature the tensile properties were found be lower than the compressive properties and this differential effects should be investigated in the future study.

14. SUBJECT TERMS
Amorphous Al alloy, Nanostructured Al alloy, Gas atomization, Melt spinning, Crystallization, Consolidation, Nanocompoiste, Nanoindentation, Mechanical properties

15. NUMBER OF PAGES

16. PRICE CODE

17. SECURITY CLASSIFICATION OR REPORT **UNCLASSIFIED**	18. SECURITY CLASSIFICATION ON THIS PAGE **UNCLASSIFIED**	19. SECURITY CLASSIFICATION OF ABSTRACT **UNCLASSIFIED**	20. LIMITATION OF ABSTRACT **UL**

NSN 7540-01-280-5500

Standard Form 298 (Rev.2-89)
Prescribed by ANSI Std. 239-18
298-102

20050711 108

1. List of Publications

1. Q. Xu and E.J. Lavernia, *Influence of nucleation and growth phenomena on microstructural evolution during droplet-based deposition.* Acta Materialia, 2001. **49**(18): p. 3849-3861.
2. S.Q. Armster, et al., *Thermo-fluid mechanisms controlling droplet based materials processes.* International Materials Reviews, 2002. **47**(6): p. 265-301.
3. B.Q. Han, E.J. Lavernia, and F.A. Mohamed, *Mechanical properties of iron processed by severe plastic deformation.* Metallurgical and Materials Transactions A, 2003. **34**(1): p. 71-83.
4. B.Q. Han, et al., *"Evaluation of Microstructure and Deformation Behavior of Pure Iron by Severe Plastic Deformation",* in Electron Microscopy: Its role in materials science, *2003 TMS Annual Meeting,* San Diego, CA, 2003. p. 209.
5. Z. Zhang, F. Zhou, and E.J. Lavernia, *On the analysis of grain size in bulk nanocrystalline materials via X-ray diffraction.* Metallurgical and Materials Transactions A, 2003. **34A**(6): p. 1349-1355.
6. Z. Zhang, D. Witkin, and E.J. Lavernia, *"Crystallization Behavior Of An Amorphous $Al_{85}Ni_{10}La_5$ Alloy",* in Processing and Properties of Structural Nanomaterials, *MS&T2003,* Chicago, IL, Nov.9-12, 2003. p. 205-212.
7. G.J. Fan, et al., *The relationship between kinetic and thermodynamic fragilities in metallic glass-forming liquids.* Philosophical Magazine, 2004. **84**(23): p. 2471-2484.
8. G.J. Fan, H.J. Fecht, and E.J. Lavernia, *Viscous flow of the Pd43Ni10Cu27P20 bulk metallic glass-forming liquid.* Applied Physics Letters, 2004. **84**(4): p. 487-489.
9. B.Q. Han, E.J. Lavernia, and F.A. Mohamed, *Dislocation structure and deformation in iron processed by equal-channel-angular pressing.* Metallurgical and Materials Transactions A, 2004. **35A**(4): p. 1343-1350.
10. B.Q. Han, F.A. Mohamed, and E.J. Lavernia, *"Deformation Behavior of Ultrafine-grained Iron Process by Equal-Channel-Angular Pressing",* in Ultrafine Grained Materials III, *2004 TMS Annual Meeting,* Charlotte, NC, March14-18, 2004. p. 413.
11. Y.J. Lin, Y.Z. Zhou, and E.J. Lavernia, *On the influence of in-situ reactions on grain size during reactive atomization and deposition.* Metallurgical and Materials Transactions A, 2004. **35A**(10): p. 3251-3263.
12. Y.J. Lin, Y.Z. Zhou, and E.J. Lavernia, *Microstructural characteristics of oxides in 5083 Al synthesized by reactive atomization and deposition.* Journal of Materials Research, 2004. **19**(10): p. 3090-3098.
13. Y.J. Lin, et al., *Thermal stability of 5083 Al synthesized by reactive atomization and deposition.* Scripta Materialia, 2004. **51**(1): p. 71-76.
14. Y.J. Lin, Y.Z. Zhou, and E.J. Lavernia, *A numerical study of oxidation behavior during reactive atomization and deposition.* Metallurgical and Materials Transactions B, 2004. **35**(6): p. 1173-1185.
15. Y.J. Lin, Y.Z. Zhou, and E.J. Lavernia, *An analytical model for the oxide size in Al alloys synthesized by reactive atomization and deposition.* Metallurgical and Materials Transactions A, 2004. **35A**(10): p. 3265-3273.
16. B.Q. Han, F.A. Mohamed, and E.J. Lavernia, *Structure and Properties of Near-nanostructured Iron,* in *Severe Plastic Deformation: Towards Bulk Production of Nanostructured Materials,* B.S. Altan, et al., Editor. 2005. in print.
17. Y.J. Lin, Y.Z. Zhou, and E.J. Lavernia, *Modeling of oxide dispersions in reactively processed Al.* Metallurgical and Materials Transactions A, 2005. **36A**(1): p. 177-186.
18. Z. Zhang, et al., *"Mechanical Properties of Amorphous $Al_{85}Ni_{10}La_5$ Alloy by Indentations",* 2005 MRS Spring Meeting, San Francisco, CA, March 28-April 01, 2005.
19. Z. Zhang, D. Witkin, and E.J. Lavernia, *Crystallization Behavior Of A Gas Atomized $Al_{85}Ni_{10}La_5$ Amorphous Alloy.* Journal of Non-Crystalline Solids, 2005. **accepted**.
20. Z. Zhang, et al., *Nanocrystal Formation in Gas-Atomized Amorphous $Al_{85}Ni_{10}La_5$ Alloy.* 2005. **to be submitted**.

2. Scientific Personnel

Mr. Zhihui Zhang, PhD student
Mr. Kit H. Foo, graduate student
Bingqiang Han, Researcher
Dr. Guojiang Fan, Post-doctoral Researcher
Dr. Yaojun Lin, Post-doctoral Researcher

3. Scientific Progress and Accomplishments

The objectives of this research program are to develop and synthesize new bulk nanostructured aluminum alloys with ultra-high strength and bulk nanostructured aluminum alloys with good wear performance for future Army systems. The research work involves the following two aspects: first, to establish an in-depth understanding of the factors that govern the synthesis and mechanical behavior of bulk nanostructured materials; second, to utilize this fundamental information to develop new bulk nanostructured aluminum alloys with high performance. This report covers the progress made during the period from September 17, 2001 to January 31, 2005. The major accomplishments through the project are summarized as follows.

3.1 Chemistry consideration of amorphous alloys

$Al_{85}Ni_{10}La_5$ (am%) was selected for the present research. The Al-TM-Ln (TM, transition metal; Ln, lanthanide) has high glass forming ability in combination with good mechanical properties. The selection of element Ni is due to its wider chemical composition range for glass forming compared with Fe and Co. The selection of element La is due to its large atomic size mismatch with Al and Ni for glass forming and the cost-effectiveness compared to other rare earth metals. Besides the glass forming ability, the thermal stability, the mechanical strength and the density of the Al-Ni-La alloy are also carefully considered for its future application. The principal considerations in determining the specific chemical compositions are summarized as follows:

(1) The $Al_{85}Ni_{10}La_5$ alloy obeys the four empirical rules for glass forming (i.e., atomic mismatch >12%, negative mixing enthalpy between the constituent components, presence of deep eutectic region, and multi-component system).
(2) The amorphous $Al_{85}Ni_{10}La_5$ alloy undergoes multi-stage crystallization events in the devitrification processes. This will allow us tailor the microstructure by controlling the crystallization kinetic conditions.
(3) After complete crystallization, this alloy consists of three equilibrium phases: Al, Al_3Ni and $Al_{11}La_3$, suggesting good thermal stability at elevated temperatures due to that no further phase transformation is expected.
(4) The fracture strength of this alloy is expected to be around 1000~1500 MPa while its theoretical density is around 3.53 g/cm^3. Figure 1 shows that the specific strength of this alloy is different from conventional engineering alloys but close to that of engineering ceramics. The unique specific strength gives this alloy good potential for future weight reduction applications.
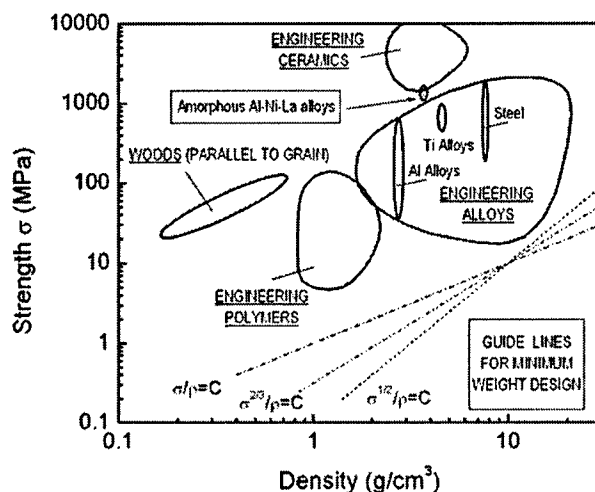
Figure 1 Strength of engineering materials plotted against density. The amorphous or partially amorphous Al-Ni-La alloys owns unique specific strength among engineering alloys for minimum weight design (M. F. Ashby, Acta Metall., Vol. 37(1989) 1273-1293).

3.2 Fabrication of Amorphous $Al_{85}Ni_{10}La_5$ Alloy

Melt spinning and gas atomization were utilized to synthesize the amorphous $Al_{85}Ni_{10}La_5$ alloy. The amorphous nature of $Al_{85}Ni_{10}La_5$ alloy was characterized using XRD, SEM and TEM. The results are concluded as follows:

(1) Amorphous $Al_{85}Ni_{10}La_5$ ribbon could be achieved with a thickness up to ~130 μm (Figure 2a);

(2) Fully amorphous $Al_{85}Ni_{10}La_5$ powders (<25 μm diameter) could be produced via gas atomization (Figure 2b);

    i) The d<25 μm powders take up 45% of over all powders produced by gas atomization.

    ii) Fine particles (d<25 μm) show smooth surface morphology. The lack of solidification shrinkage on the spherical surface reveals the amorphous nature of the particles (Figure 4a). The presence of solidification shrinkage on the coarse particles (d>25 μm) indicates that crystallization has taken place in these particles (Figure 4b).

    iii) The cross-section view of the d<25 μm powders is shown in Figure 5(a). For comparison, the as-cast microstructure of $Al_{85}Ni_{10}La_5$ alloy is shown in Figure 5(b). The BSE image in Figure 5(a) shows a featureless microstructure in contrast to the typical eutectic microstructure shown in Figure 5(b). Figure 5(a) shows that tiny intermetallic phases (d<1 μm) could also be observed in some of the particles but the volume fraction is estimated to be <1%.

    iv) The TEM micrographs for the d<25 μm powders are given in Figure 6, confirming their amorphous nature. However, it was found that nanocrystallization had occurred with a grain size <100 nm in some particles during the solidification process, as shown in Figure 7. It should be mentioned that crystalline phase in the d<25 μm powders is not detectable by XRD, suggesting that the crystalline fraction is less than 2% (The detectability of XRD in this particular alloy is ~2%).
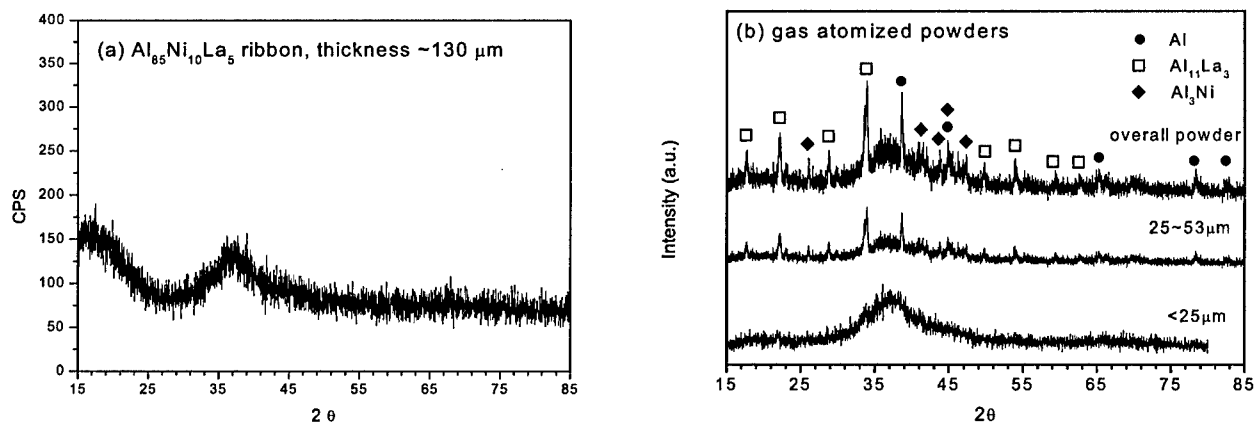
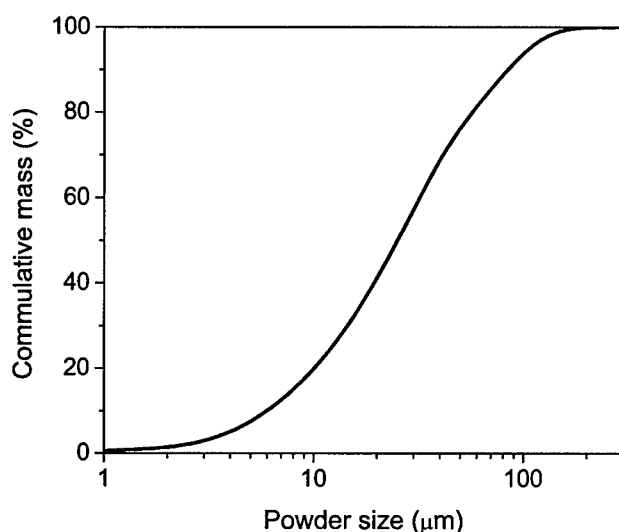Figure 2 XRD profile of $Al_{85}Ni_{10}La_5$ alloy. The ribbons were tested on the reverse-to-wheel side (shining side).

Figure 3 Cumulative size distribution of the gas atomized $Al_{85}Ni_{10}La_5$ powders. The <25 μm powders taking up 45% of over all powders produced by gas atomization.

Figure 4 SEM micrographs of the gas atomized $Al_{85}Ni_{10}La_5$ powders: (a) fine particles exhibit smooth surface and the indents are caused by collision among the particles (Left); and (b) coarse particles exhibit rough surface due to solidification shrinkage (Right).
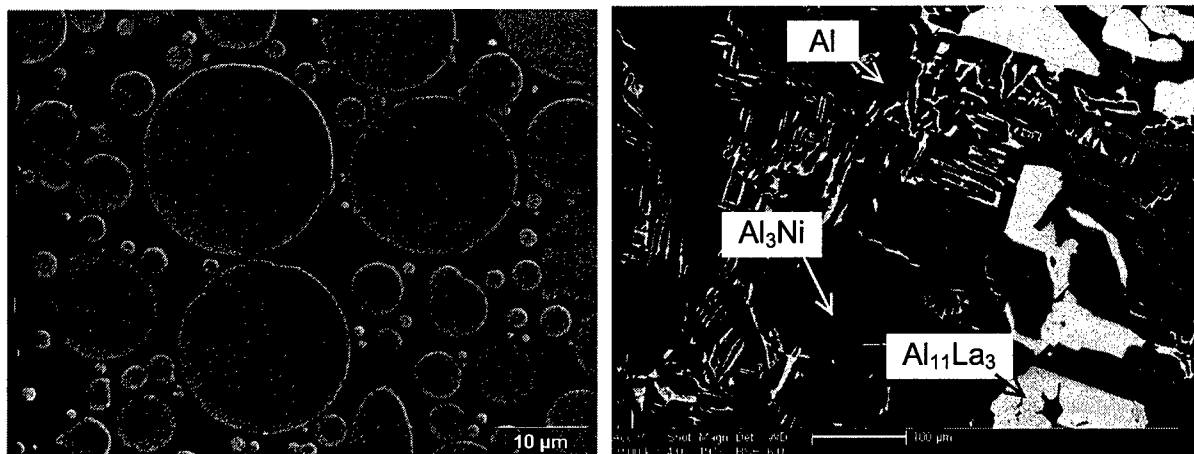
Figure 5 Back scattered electron images for as-atomized $Al_{85}Ni_{10}La_5$ powders (<25 μm) (a) and as-cast $Al_{85}Ni_{10}La_5$ ingot (b).
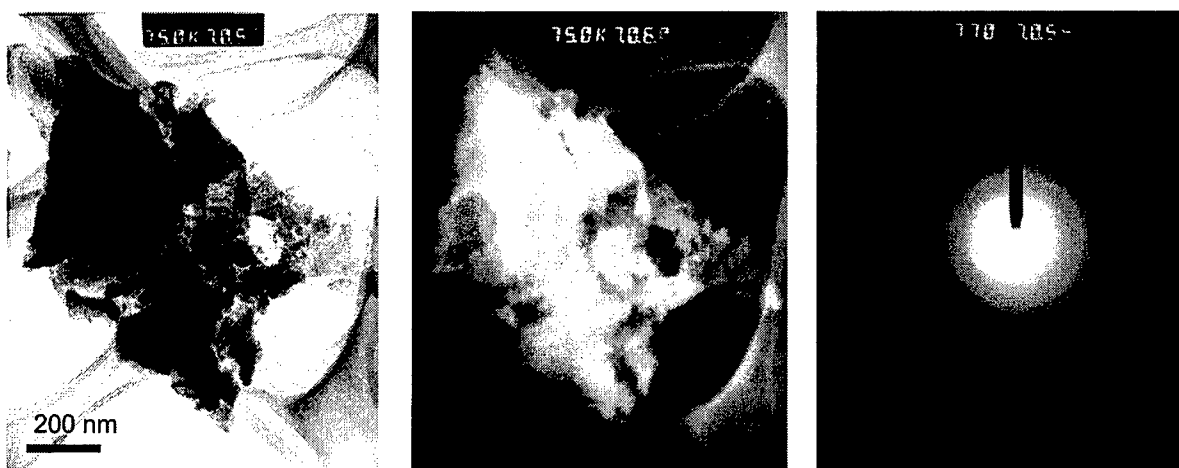
Figure 6 TEM micrographs for as-atomized $Al_{85}Ni_{10}La_5$ powders (<25 μm): (a) bright filed image, (b) dark filed image, and (c) the selected area diffraction pattern
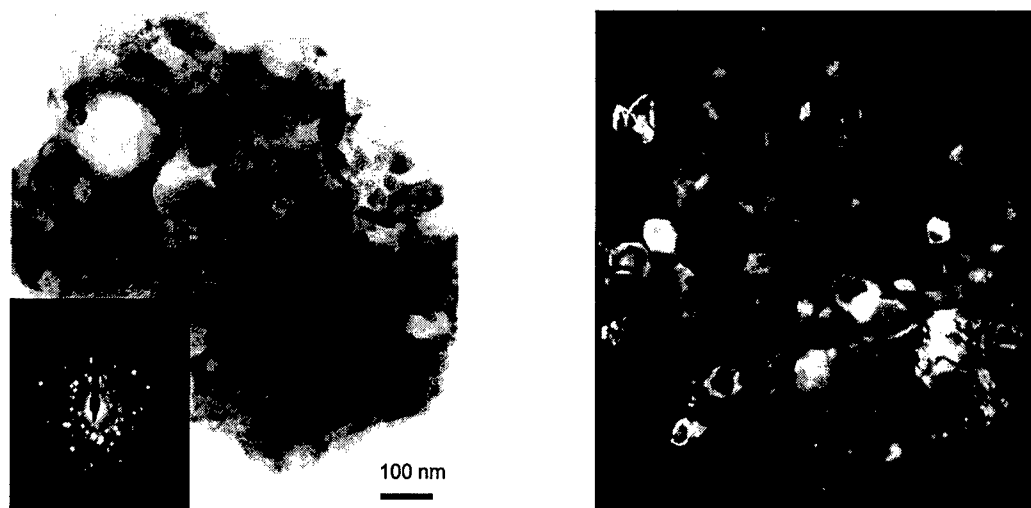
Figure 7 TEM micrographs of nanocrystalline $Al_{85}Ni_{10}La_5$ powders (< 25 μm). (a) Bright field image (left); (b) Dark field images (right); and (c) Selected area diffraction pattern inset in (a).

3.3 Crystallization Behavior and Kinetics of Amorphous $Al_{85}Ni_{10}La_5$ Alloy

3.3.1 Temperature scans

Findings by DSC continuous tracing are summarized (Figure 8):
(a) Similar crystallization behavior was found both in gas atomized powders and melt spun ribbons.
(b) Clearly divided multi-stages of crystallization were identified, providing a potential to control the crystallization progress, and in turn, may facilitate the subsequent consolidation process.
(c) Distinct glass transition, at a heating rate of 40 °C/min, $T_g \approx 259$ °C.
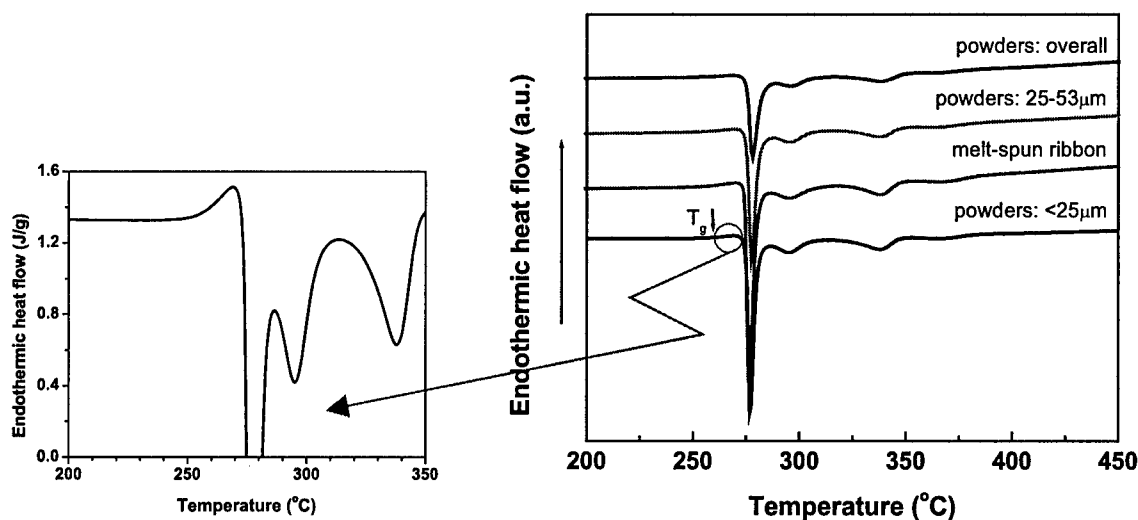
Figure 8 DSC continuous tracing curves of $Al_{85}Ni_{10}La_5$ alloy.

3.3.2 Kissinger analysis

The thermal activation energy for the crystallization reactions was determined by Kissinger analysis. Results, obtained by fitting the exothermic peak temperature to the Kissinger equation, are shown in Figure 9. The activation energy for the first peak is approximately E_a=344 KJ/mol. However, the self-diffusion activation energy of Al is Q=144.2 KJ/mol, which is far below the activation energy E_a=344 KJ/mol. It suggests that the presence of the element La and Ni in the amorphous matrix considerably influences precipitating of Al. This may account for the high glass transition point of $T_g \approx 259$ °C (> $0.55T_M$). The second peak does not exhibit a linear relation and this probably because the reactions are sensitive to temperatures and thus the activation energies are temperature dependent.
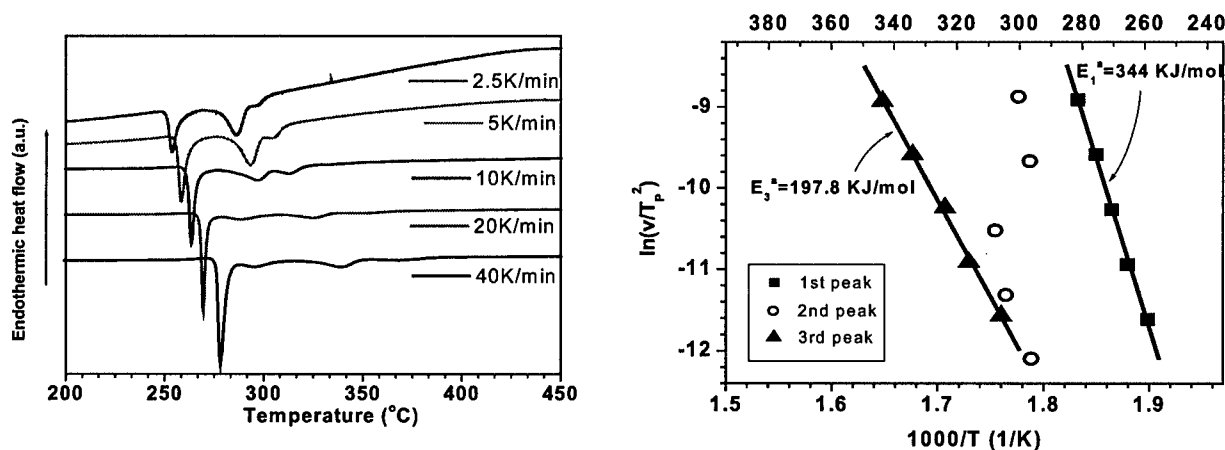
Figure 9 Kissinger plots for gas atomized $Al_{85}Ni_{10}La_5$ powders (<25 μm).

3.3.3 Isothermal annealing

Results of isothermal annealing are shown in Figure 10. Please note that sample A was annealed at 235 °C for 60 min, sample B at 245 °C for 30 min and sample C at 250 °C for 30 min, and then heated at 40 °C /min to 500 °C. Figure 10(b) shows the DSC continuous scans of the partially crystallized samples A, B and C in Figure 10(a) respectively. It can be seen that the first crystallization peak for sample A remains in Figure 10(b) after the annealing at 235 °C, whereas the first crystallization peaks could not be resolved in sample B and C in Figure 10(b) after the isothermal annealing at 245 °C and 250 °C respectively. Furthermore, careful examination of the isothermal peaks in Figure 10(a) suggests the following crystallization mechanisms:

(1) The isothermal calorimetry signal at 235 °C showing a monotonically decreasing curve suggests a growth of quenched-in nuclei existing in the amorphous matrix;

(2) The presence of a peak at 245 °C and 250 °C suggests that a nucleation and growth process occurs. Meanwhile, the presence of an apparent incubation period at 245 °C and 250 °C indicates that the nuclei were newly created during the incubation period and different from the quenched-in nuclei observed at 235 °C.
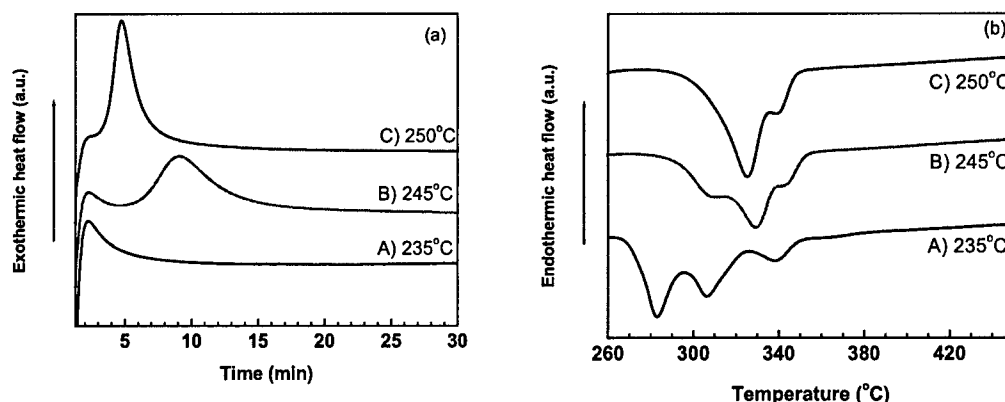
Figure 10 Isothermal annealing of gas atomized $Al_{85}Ni_{10}La_5$ powders (<25 μm).

3.3.4 The Johnson-Mehl-Avrami (JMA) model

The isothermal calorimetry signals in Figure 10(a) were further analyzed using the Johnson-Mehl-Avrami (JMA) model. From Figure 10(a), the transformed volume fractions vs. the annealing time is shown in Figure 11(a) and the Avrami plots of $\ln(-\ln(1-\zeta))$ vs. $\ln(t)$ are given in Figure 11(b). The various Avrami exponents at different temperatures further reveal the following crystallization mechanisms for the amorphous alloy:

(1) The Avrami exponents at 245 °C are equal to 3.3 at the initial stage and then decrease to 1.9 at the final stage. In the case of 250 °C, the Avrami exponent starts at 3.9 before finally decreasing to 1.7. The non-linear nature of the Avrami plots implies that the transformation mechanisms have changed in the final crystallization stage, i.e., from interface-controlled transformation to diffusion-controlled transformation.

(2) The Avrami exponent at 235 °C is less than 1 and it is evidence of growth from pre-existing nuclei.
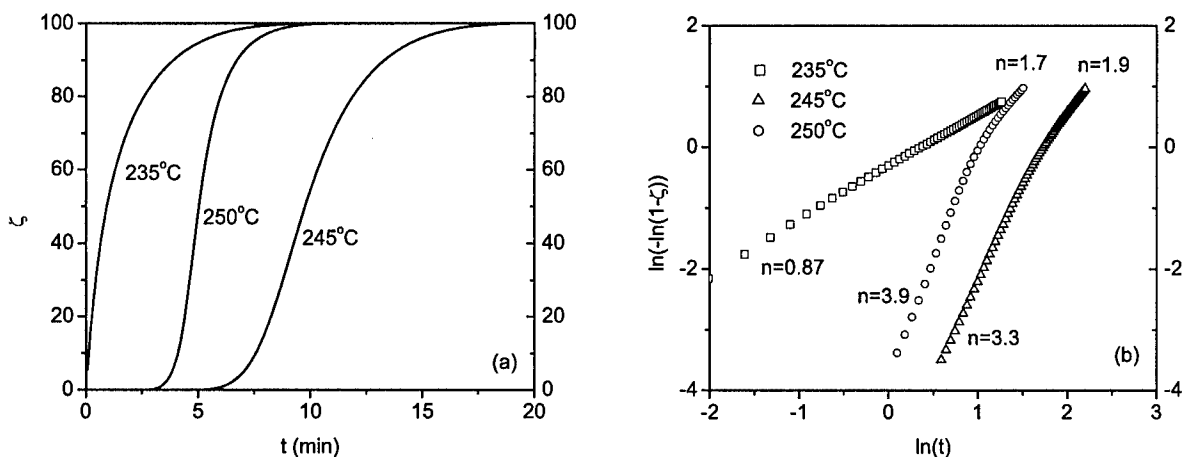
Figure 11 Plots of transformed volume fraction vs. annealing time (a) and the Avrami plots (b)
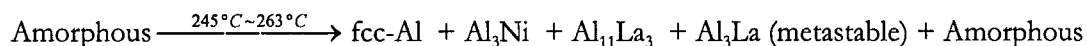
3.3.5 Nanocrystalline phases development at various temperatures

Development of nanocrystalline phases during the devitrification process was studied by annealing the amorphous powders below glass transition temperature (i.e., 235 °C, 245 °C and 250 °C for 30 min) and above glass transition temperature (i.e., 263 °C and 283 °C for 5 min). XRD and TEM were used to identify the phase composition and grain sizes. The results are summarized as follows:

(a) As discussed before, a growth reaction occurs at 235 °C; XRD analysis of the powder sample annealed at 235 °C shows that the reaction corresponds to the growth of fcc-Al phase, as shown in Figure 12. TEM observation indicated that grain size of the fcc-Al nanocrystal is around 10 nm, as shown in Figure 13(a).

$$\text{Amorphous} \xrightarrow{235°C} \text{fcc-Al} + \text{Amorphous}$$
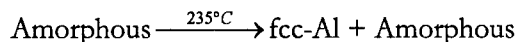
(b) At 245 °C, Al phase and intermetallic compounds of $Al_{11}La_3$ and Al_3Ni precipitated in a eutectic-like reaction. In addition, a minor metastable phase Al_3La was also observed in the XRD pattern (Figure 12). At temperatures of 250 °C and 263 °C, the same phases were identified in the XRD pattern. The formed nanocrystalline phases homogeneously distributed in the amorphous matrix, as shown in Figure 13(b) and (c), with a grain size around 20 nm.

$$\text{Amorphous} \xrightarrow{245°C\sim263°C} \text{fcc-Al} + Al_3Ni + Al_{11}La_3 + Al_3La \text{ (metastable)} + \text{Amorphous}$$

(c) At 283 °C, the minor metastable phase Al_3La was dissolved (Figure 12). The microstructure exhibits bimodal distribution, with the lower bound grain size of ~20 nm and the upper bound grain size of ~100 nm (Figure 13d).
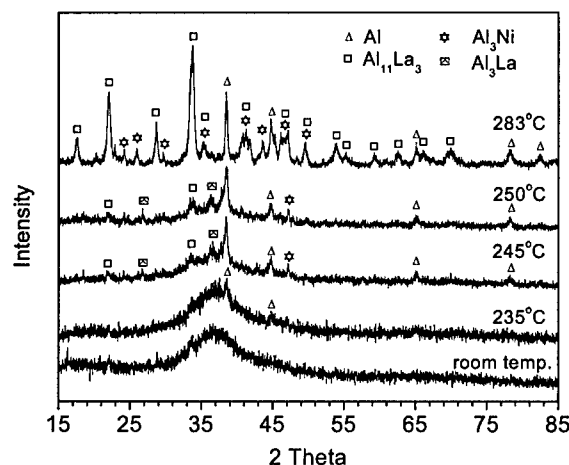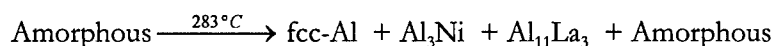
$$\text{Amorphous} \xrightarrow{283°C} \text{fcc-Al} + Al_3Ni + Al_{11}La_3 + \text{Amorphous}$$

Figure 12 XRD patterns of $Al_{85}Ni_{10}La_5$ powders (<25μm) annealed at various temperatures.

3.3.6 SAXS study of the partially crystallized microstructure

The partially crystallized amorphous powders possess a microstructure with nanoscale precipitates embedded in the remaining amorphous matrix. Findings about the nanoscale precipitates using small angle X-ray scattering (SAXS) include:

(a) The scattering intensity for the powders annealed at 245°C or 250°C is higher than that for 235°C, indicating an increase of scatterers in the disordered background, suggesting a higher fraction of crystallites precipitated from the matrix at 245°C or 250°C. This is in agreement with the heat release at the different temperatures determined using DSC.

(b) Figure 14(a) revealed that the nanoscale crystallites exhibited a bimodal distribution. In the Guinier's plot of $\ln(I)$ vs. q^2, the gyration of radii are determined as $R_g^1 = 18.3$ nm and $R_g^2 = 6.1$ nm, corresponding to an averaged particle size of 47 nm and 16 nm, respectively. Occurrence of the smaller particles attributed to precipitation of nanoscale particles in the amorphous matrix. However, the larger particles could not attribute to the partial devitrificaton process, because they were formed during the atomization and solidification process (see Figure 7).

(c)   As seen in Figure 14(b), the slope in the logarithmic power-law plots approaching ~4 indicates that a sharp interface exists between the particles and matrix. This result suggests that the crystallization event is a thermally activated process instead of phase separation.

(d)   The bimodal distribution of crystallites in the amorphous matrix was in good agreement with TEM observations. Figure 7 shows that crystallization occurred during the solidification process in the as-atomized powders with a grain size of around 50nm. It should be mentioned that these crystalline phases were not detected in the XRD pattern. Figure 13(b) shows that smaller particles of around 20 nm precipitated during annealing at 245°C.
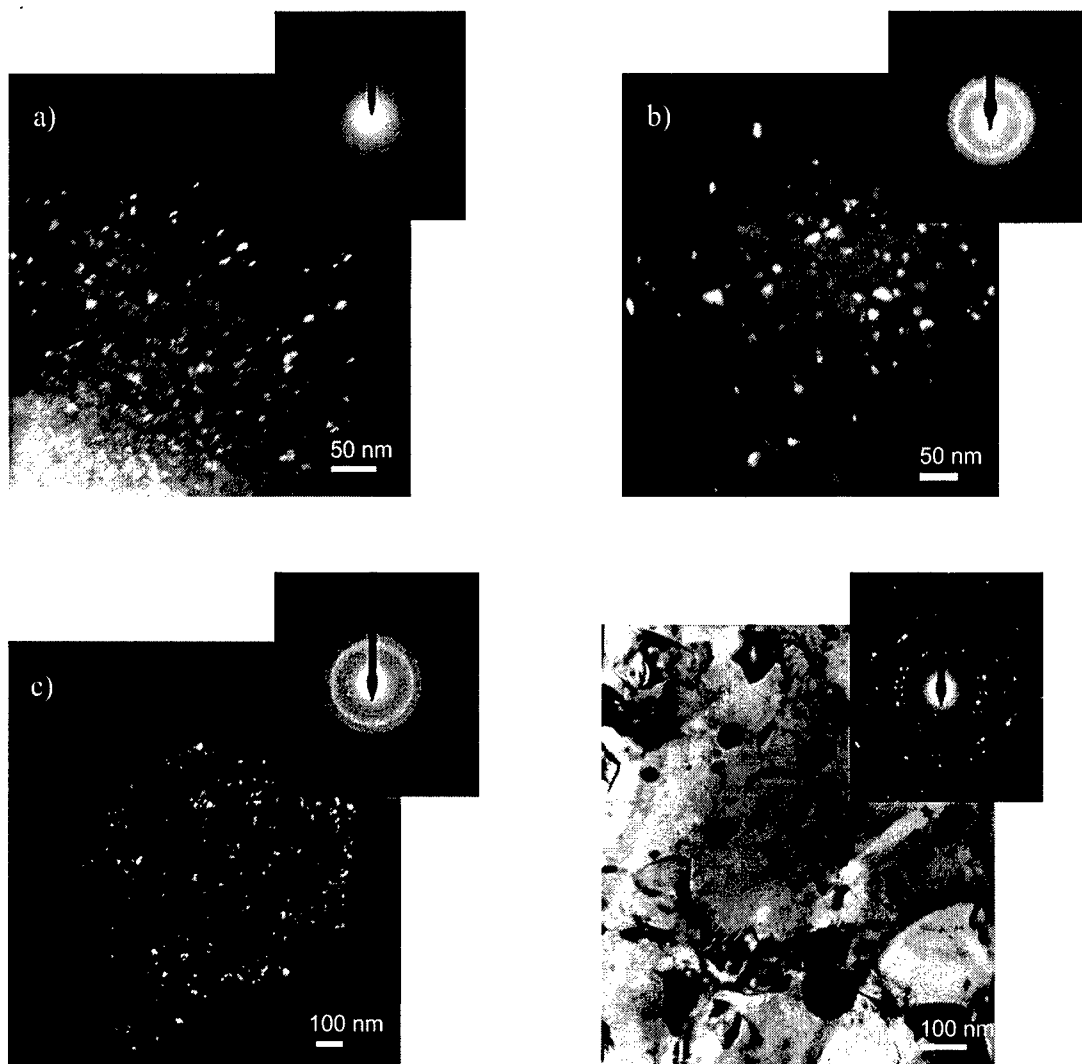
Figure 13 TEM micrographs for partially crystallized amorphous $Al_{85}Ni_{10}La_5$ alloy at various temperatures: (a) 235 °C, (b) 245 °C, (c) 263 °C, (d) 283 °C.
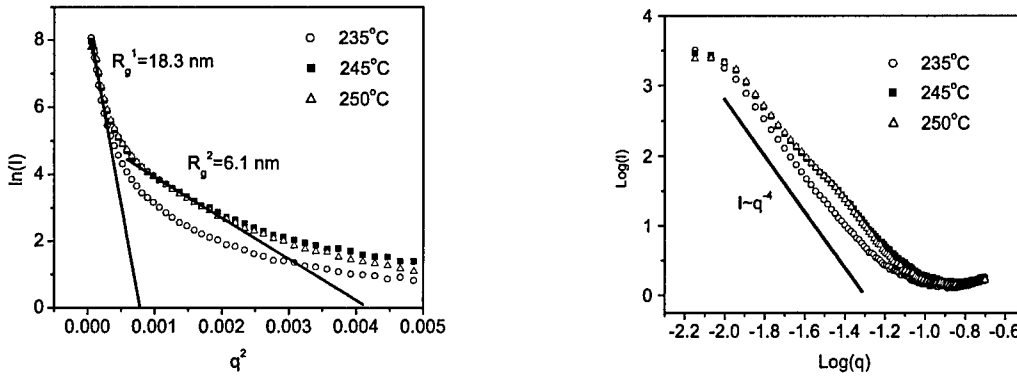
Figure 14 SAXS scattering patterns for an $Al_{85}Ni_{10}La_5$ amorphous alloy annealed for 30 min at 235°C, 245°C and 250°C respectively. (a) Guinier' plot ln(I) vs. q^2 , (b) power law plot log(I) vs. log(q).

3.4 Thermal Stability and Grain Growth of the $Al_{85}Ni_{10}La_5$ Alloy

A temperature of 300 °C or higher is necessary to consolidate the amorphous powders into bulk material. However, the consolidation process at 300 °C could lead to rapid coarsening of the microstructure. In the present study, the influence of annealing temperature on the thermal stability of the amorphous alloy was studied. Experimental results are described as follows:

(1) Pre-annealing at 235 °C (growth of fcc-Al)

> i)   After holding at 283 °C for 5 min, more amorphous phase remained due to pre-annealing at 235 °C for 1 hr compared with the sample without pre-annealing. (Figure 14);
>
> ii)   Presence of Al_3La implies that the microstructure has not been fully evolved, indicating that the stability is enhanced by means of pre-annealing (Figure 14);
>
> iii) With an increasing of the pre-annealing time from 30 min to 60 min, the peak temperature for the first reaction shifts from 277 °C to 283 °C. This suggested that growth of fcc-Al helps to stabilize the amorphous matrix (Figure 15).
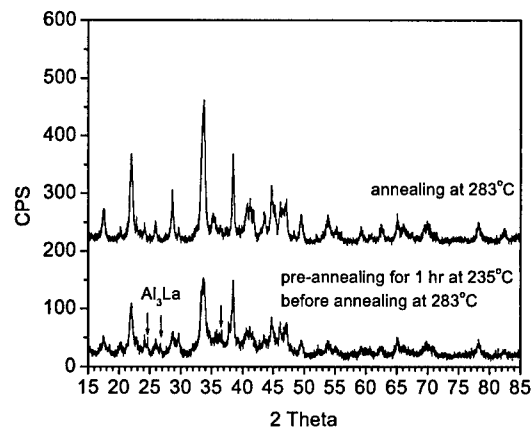
Figure 14 XRD pattern demonstrating the effects of pre-annealing
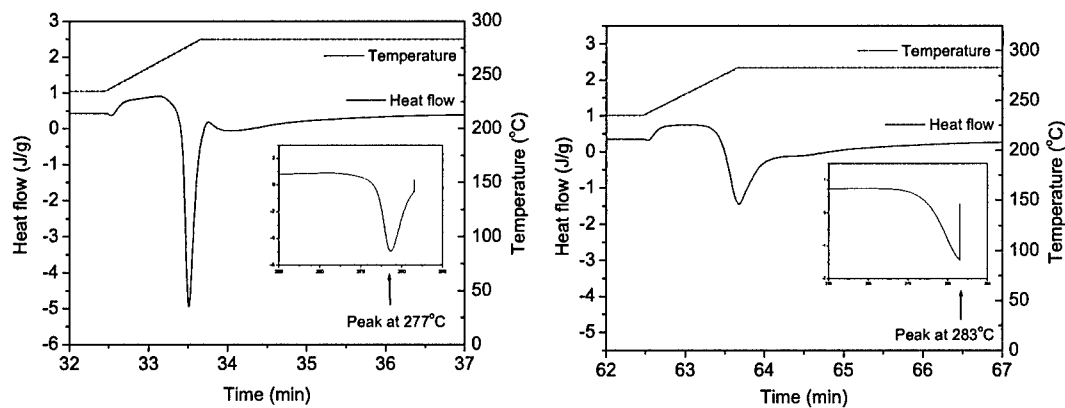
Figure 15 DSC curve demonstrating the effects of pre-annealing (at a heating rate of 40°C/min).

(2) Annealing at 250 °C (eutectic crystallization)

- i)   When annealing at 250 °C for 0.5 hr, the grain size is about 20 nm, as shown in Figure 16(a, b);
- ii)   When annealing at 250 °C for 3 hr, the grain size is about 25 nm, as shown in Figure 16(c, d);
- iii)   When annealing at 250 °C for 6 hr, the grain size is about 40 nm;
- iv)   The coarsening of fcc-Al nanocrystals at 250 °C exhibits an exponent of approximately 3, as shown in Figure 17.
- v)   When annealed at 250 °C for 6 hr and followed by holding at 268 °C for 3 hrs, no significant growth was observed compared with the microstructure under treatment (iii), as shown in Figure 16(e, f).
- vi)   When annealed at 250 °C for 6 hr and followed by holding at 268 °C for 6 hr, a heterogeneous microstructure formed, as shown in Figure 16(g, h).

(3) Annealing at 280 °C

- a)   When annealing at 280 °C for 3 hr, the grain size is about 200 nm, as shown in Figure 16(i);
- b)   When annealing at 280 °C for 6 hr, the grain size is about 300 nm, as shown in Figure 16(j).

In summary, low temperature annealing (e.g., <268 °C) helps improving the thermal stability. This could be attributed to the high nucleation density (estimated as $\sim 10^{21 \sim 22}/m^3$) and therefore the Al, Al_3Ni and $A_{11}1La_3$ phase did not form lamellar structure. After the amorphous alloy undergoes low temperature annealing, the free energy of the alloy has been decreased and the microstructure coarsening would be at expense of smaller grains, this process would however require long-range diffusion of the atom La and Ni. As a consequence, the thermal stability was improved. On the contrary, if crystallization occurs at high temperatures (>280 °C), the driving force mainly arises from the free energy change from the amorphous state to the crystalline state, which could result in higher atomic migration rate.
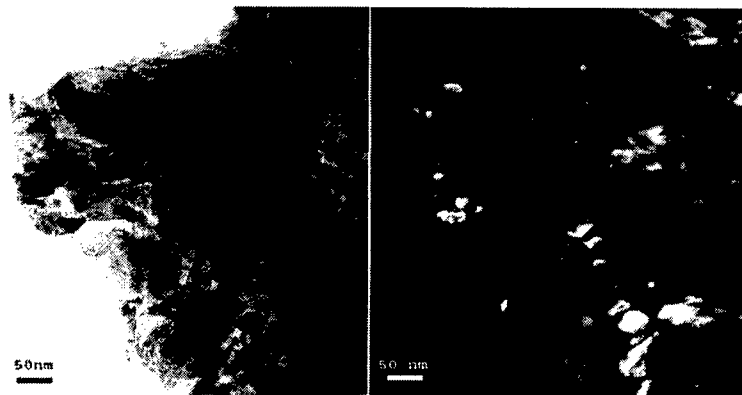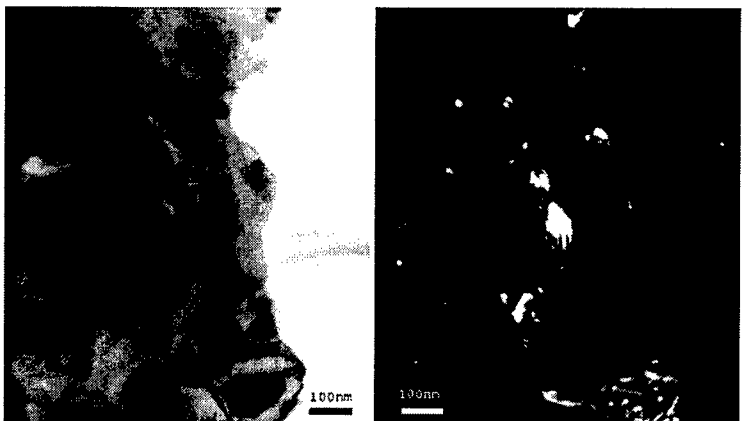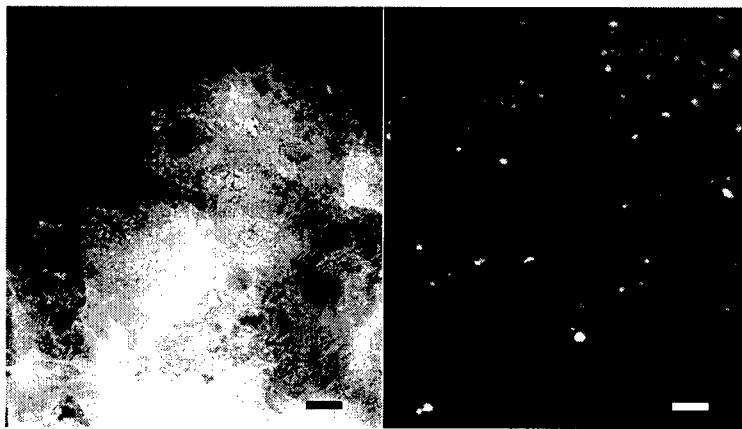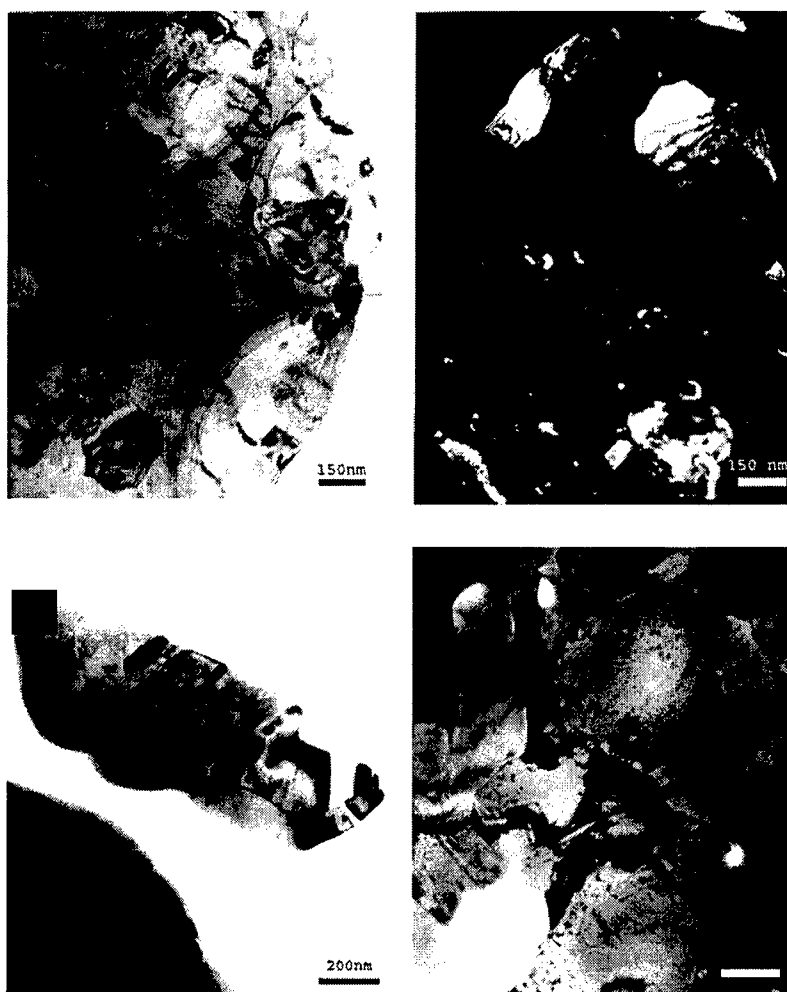
Figures 16 Microstructure of $Al_{85}Ni_{10}La_5$ Powders (<25 μm) that were heat treated at various temperatures.
Bright field (a) and dark field (b) images for the amorphous powders treated at 250 °C for 0.5 hr;
Bright field (c) and dark field (d) images for the amorphous powders treated at 250 °C for 3 hr;
Bright field (e) and dark field (f) images for the amorphous powders treated at 250 °C for 6 hr and followed by holding at 268 °C for 3 hr;
Bright field (g) and dark field (h) images for the amorphous powders treated at 250 °C for 6 hr and followed by holding at 268 °C for 6 hr;
Bright field (i) image for the amorphous powders treated at 280 °C for 3 hr;
Bright field (j) image for the amorphous powders treated at 280 °C for 6 hr;
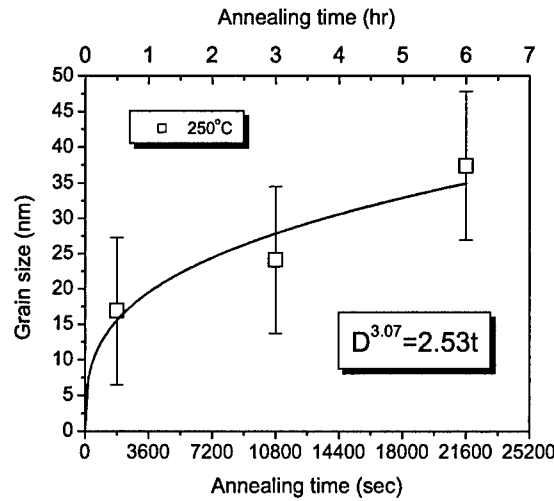
Figure 17 Coarsening of fcc-Al nanocrystal at 250 °C in $Al_{85}Ni_{10}La_5$ powders (<25 μm).

3.5 Indentation Study of the Mechanical Properties of Partially Crystallized $Al_{85}Ni_{10}La_5$ Powders

3.5.1 Microhardness

Results of microhardness testing of the amorphous and partially crystallized $Al_{85}Ni_{10}La_5$ powders (<25 μm) were summarized as follows:

(a) Partially crystallized amorphous $Al_{85}Ni_{10}La_5$ alloy has higher mechanical properties than the amorphous counterpart, as seen in Figure 18(a);

(b) Figure 18(b) shows the variation of hardness vs. transformed volume fraction by re-plotting Figure 18(a). The transformed volume could be determined by measuring the residual areas in the continuous temperature scan after the annealing event.

$$V_f = \frac{\Delta H_T - \Delta H_R}{\Delta H_T}$$

where ΔH_T is the total enthalpy released upon complete crystallization. ΔH_R is the total remnant enthalpy released upon crystallization of the partially crystallized sample. The linear relationship suggests that the increasing of microhardness complies with rule of mixing. In other words, the partially crystallized alloy can be regarded as a nanocomposite with nanocrystals embedded in the amorphous matrix. After the treatment at 283°C, however, the hardness did not increase further. This could be attributed to the rapid growth of the nanocrystals at this temperature, whereby, eventually the Hall-Petch effect becomes dominant in this alloy.

(c) Around the indent the amorphous sample (Figure 19a) exhibits pile-ups in a manner of stepped arcs, suggesting the formation of shear bands. Comparing Figure 19(b) with 19(a), one can see that the presence fcc-Al nanocrystal in the sample treated at 235°C promotes formation of multiple shear bands. However, the sample treated at 250°C (Figure 19c) exhibited much smaller pileups, suggesting this alloy exhibits unusual deformation behavior; meanwhile, no cracks around the indent are observed, indicating that the $Al_{85}Ni_{10}La_5$ alloy at this state is not fully brittle.
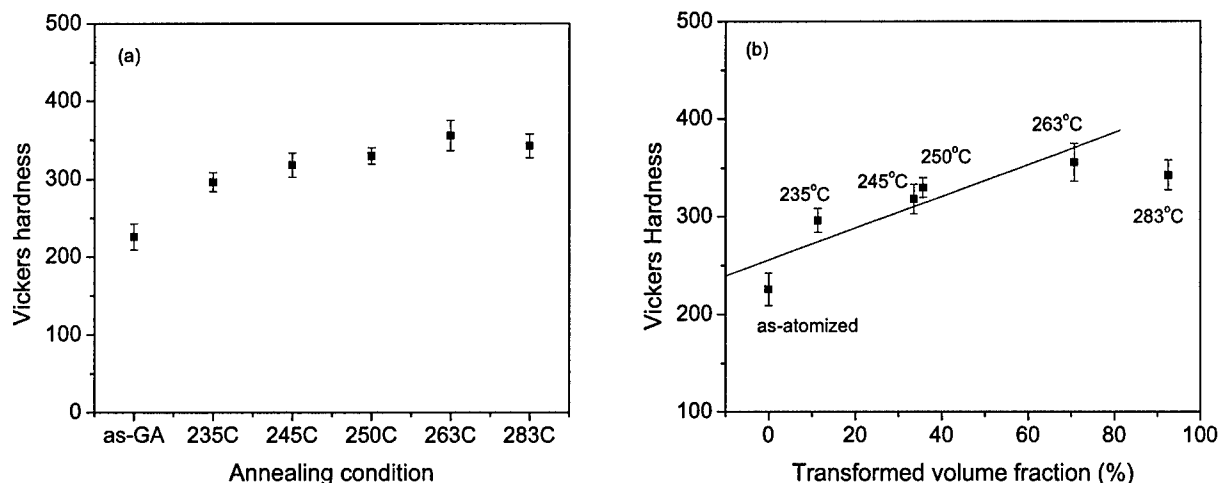
Figure 18 Microhardness of the $Al_{85}Ni_{10}La_5$ powders: (a) variation of hardness vs. annealing temperature; (b) variation of hardness vs. transformed volume fraction.

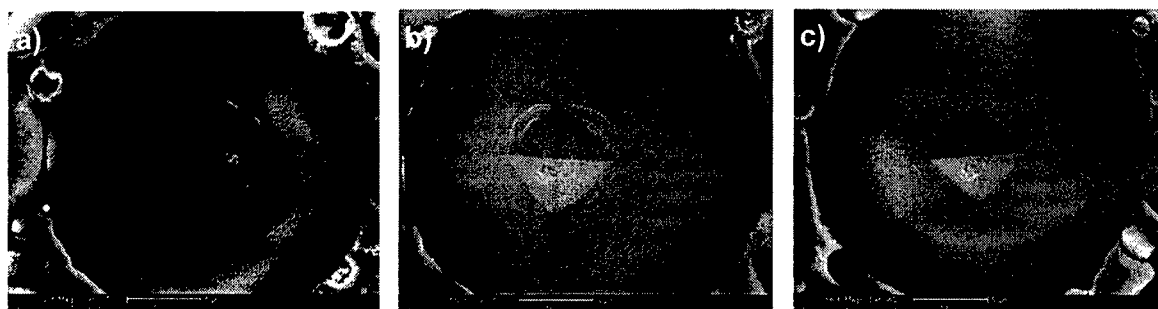Figure 19 SEM images for indentations on $Al_{85}Ni_{10}La_5$ powders (<25μm). (a) as-atomized (b) treated at 235°C for 30 min (c) treated at 250°C for 30 min

3.5.2 Nanoidentation

Microhardness testing is limited to relatively large particles (close to 25μm). However, nanoidentation allows measuring finer particles as well as the elastic modulus of this alloy. Results of nanoidentation are shown in Figure 20, indicating that:

(a) Hardness increased due to partially crystallization. The hardening behavior is similar to Figure 18. Again, after the treatment at 283°C, the hardness did not increase further. When this alloy is consolidated into bulk form, the hardness decreases further due to further growth. Details about the bulk material will be discussed in next section.

(b) Elastic modulus was also increased due to partially crystallization. The modulus of the amorphous Al alloy is slightly lower than the conventional modulus for Al alloy (70~79 Gpa).
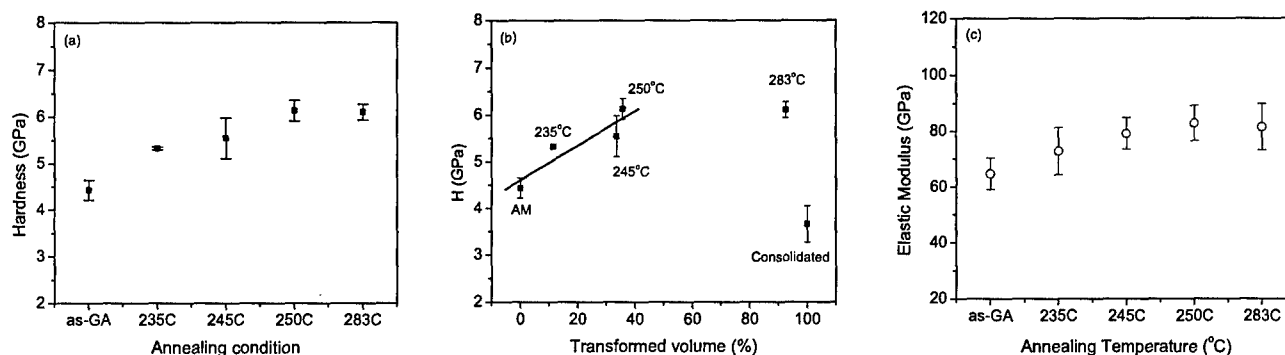
Figure 20 Nanoidentation results of the $Al_{85}Ni_{10}La_5$ alloy powders. (a) Hardness vs. temperature; (b) Hardness vs. transformed volume fraction; (c) Elastic modulus

3.6 Mechanical Properties of Bulk Materials

Amorphous $Al_{85}Ni_{10}La_5$ powders and cryomilled 5083 Al powders were mixed and then consolidated via cold isostatic pressing (CIP) followed by degassing and extrusion. The composites with 10 vol.% and 20 vol.% $Al_{85}Ni_{10}La_5$ powders respectively were used to study the mechanical properties. The addition of cryomilled 5083 Al alloy is for the purpose of further reducing the density of bulk material but still keeping high strength. For example, the density of bulk material containing 20 vol.% $Al_{85}Ni_{10}La_5$ is estimated to be only ~2.9 g/cm³. In addition, effect of swaging, annealing or HIP'ing on the mechanical properties of the as-extruded materials was also studied.

3.6.1 Microstructure

Optical observation shows that the $Al_{85}Ni_{10}La_5$ powders are uniformly distributed in the 5083 Al matrix (Figure 21a). SEM observation shows that the amorphous $Al_{85}Ni_{10}La_5$ powders are homogeneously crystallized during the consolidation process and the crystallized phases have a grain size around 100~200 nm, as shown in Figure 21(b) and (c). TEM observation confirms the value of grain size estimated by SEM, as shown in Figure 21(d).

3.6.2 Test specimens

The bulk composite materials were machined into flat dog-bone tensile specimens along the extrusion direction, with the gage length of 12 mm, width of 4 mm, and thickness of 2 mm. The gage sections of the tensile specimens were polished close to a mirror finish. Compression specimens were machined along the extrusion direction, with a size of $\phi 4 \times 5$ mm.

3.6.3 Compressive properties

Results of the compression properties are shown in Figure 22, showing that:
(a) The $Al_{85}Ni_{10}La_5$ particles function as a reinforcement source, increasing of strength complies with rule of mixing.
(b) The as-extruded 10 vol.% $Al_{85}Ni_{10}La_5$ specimen has a compressive strength >800 MPa; the as-extruded 10 vol.% $Al_{85}Ni_{10}La_5$ sample particles has a compressive strength larger than 1000MPa, but has limited ductility.
(c) Swaging could increase the ductility of the 10 vol.% $Al_{85}Ni_{10}La_5$ composite significantly without losing the strength. The fracture strain could reach as high as around 0.25.
(d) Examination of the fracture surface shows that the failure is due to debonding between the $Al_{85}Ni_{10}La_5$ particles and the matrix. As shown in Figure 23, the friction scratch caused by particles pulling out is clearly seen.

3.6.4 Tensile properties

In tensile tests, the bulk material failed before yielding. The tensile strength shows large differential effect compared with the compressive strength. This could be attributed to the weak bonding strength between the $Al_{85}Ni_{10}La_5$ particles and matrix. The influence of annealing, HIP'ing and swaging on the ductility was studied. Results show that the fracture strength could be improved, as shown in Figure 24.
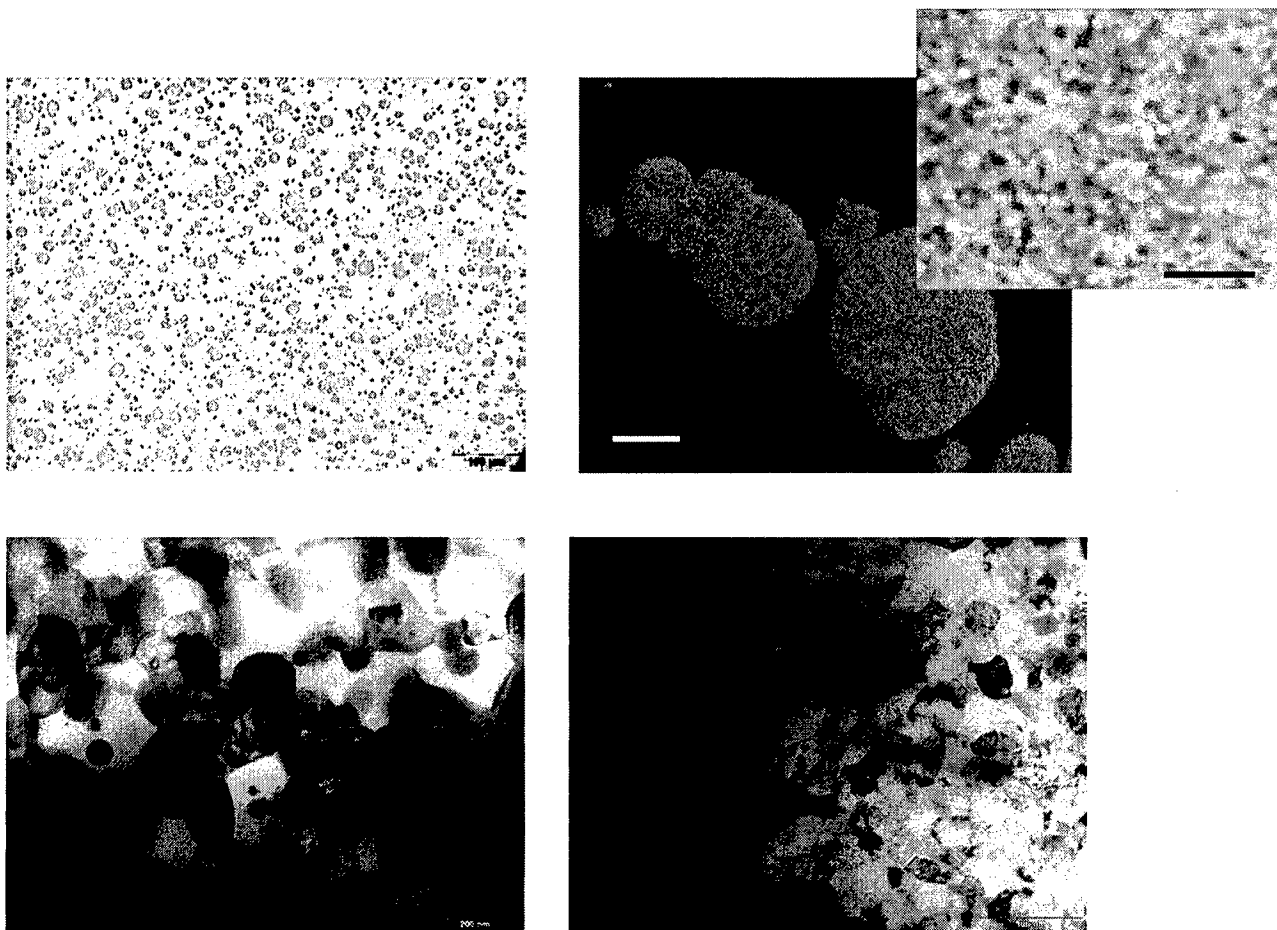
Figure 21 Microstructure of the composite with 20vol.% $Al_{85}Ni_{10}La_5$: (a) homogeneous distribution of the $Al_{85}Ni_{10}La_5$ particles (optical image); (b) and (c) BSE image of the $Al_{85}Ni_{10}La_5$ particles; (d) TEM bright filed image of $Al_{85}Ni_{10}La_5$ particles; (e) TEM bright field images of the 5083 Al matrix.

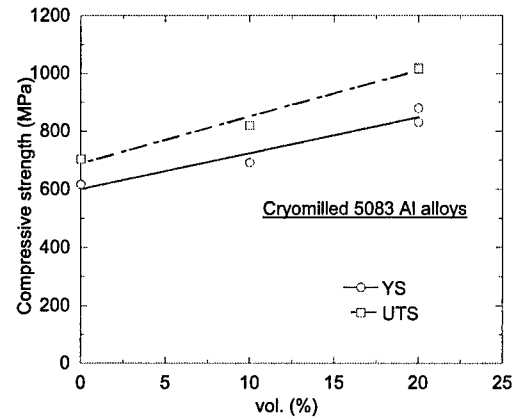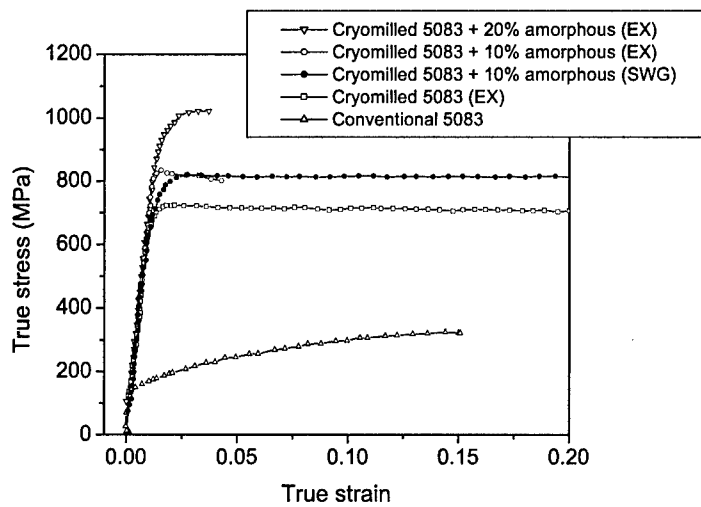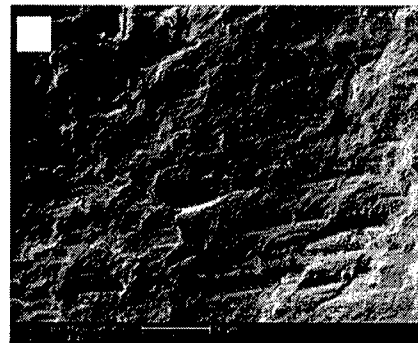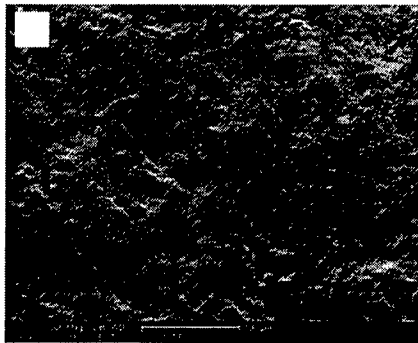Figure 22 Mechanical properties the composite with $Al_{85}Ni_{10}La_5$: (a) Stress vs. strain curve (b) strength vs. volume fraction of the $Al_{85}Ni_{10}La_5$ particles.

Figures 23 Fracture surface after compressive testing of the as-extruded composite containing 10 vol.% $Al_{85}Ni_{10}La_5$ particles (a) and 20 vol.% $Al_{85}Ni_{10}La_5$ particles (b).
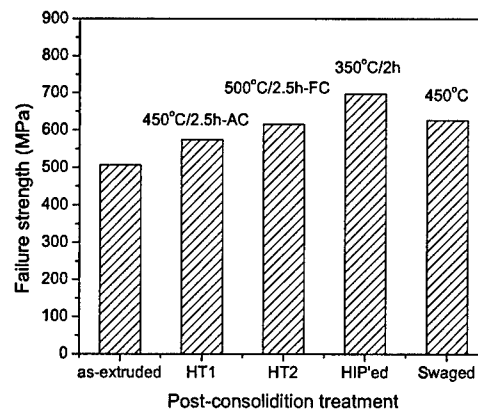
Figure 24 Influence of post-consolidation treatment to the fracture strength of $Al_{85}Ni_{10}La_5$ /5083 Al composite

3.6.5 Mechanical properties at elevated temperatures

The $Al_{85}Ni_{10}La_5$ /5083 Al composite shows promising high temperature properties. As shown in Figure 25, both the compressive and tensile tests indicated that the fracture strength at 200°C can reach ~400 MPa.
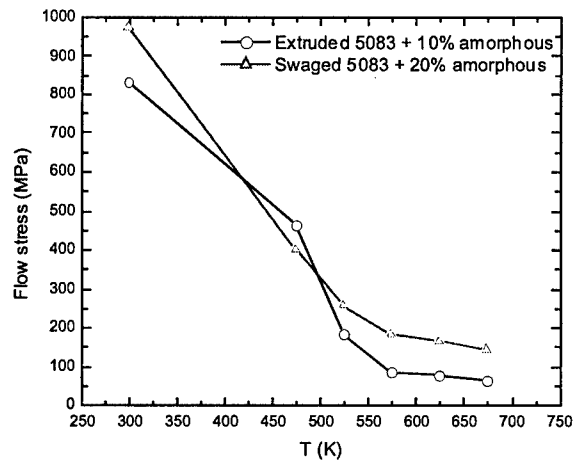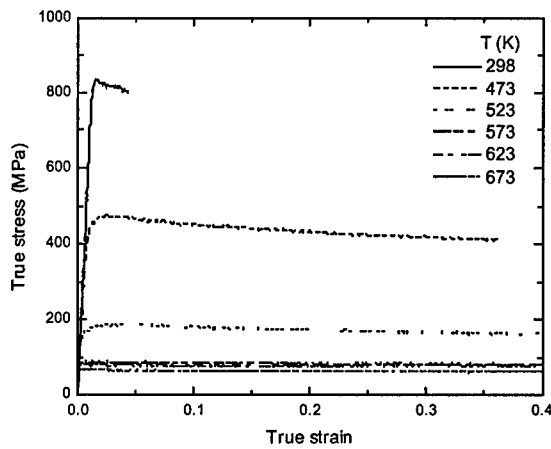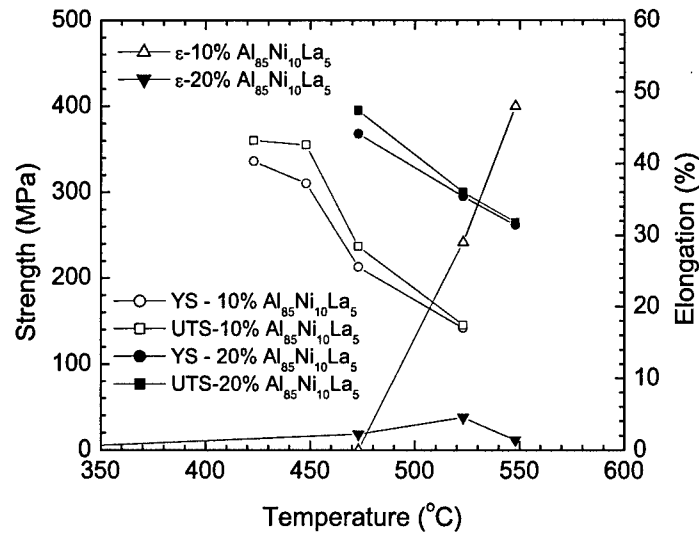

Figure 25 High temperature properties of the $Al_{85}Ni_{10}La_5$ /5083 Al composite: (a) tensile strength and elongation vs. temperature; (b) compressive stress vs. strain curve; (c) compressive flow stress vs. temperature.

In the previous sections, amorphous $Al_{85}Ni_{10}La_5$ powders made by gas atomization have been used for consolidation into bulk material. However, the yield rate for full amorphous powders is ~45%. Alternatively, the probability of fragmenting ribbons into equiaxed powders by mechanical milling was investigated. However, mechanical milling could not only change the morphology, but also change the microstructure of the ribbons. In order to characterize the microstructure evolution of the amorphous ribbons, partially amorphous $Al_{85}Ni_{10}La_5$ ribbons were milled using high energy ball milling. Preliminary results show that (Figure 26, Figure 27):

(1)   Balling can effectively fragment the partially amorphous $Al_{85}Ni_{10}La_5$ ribbons;

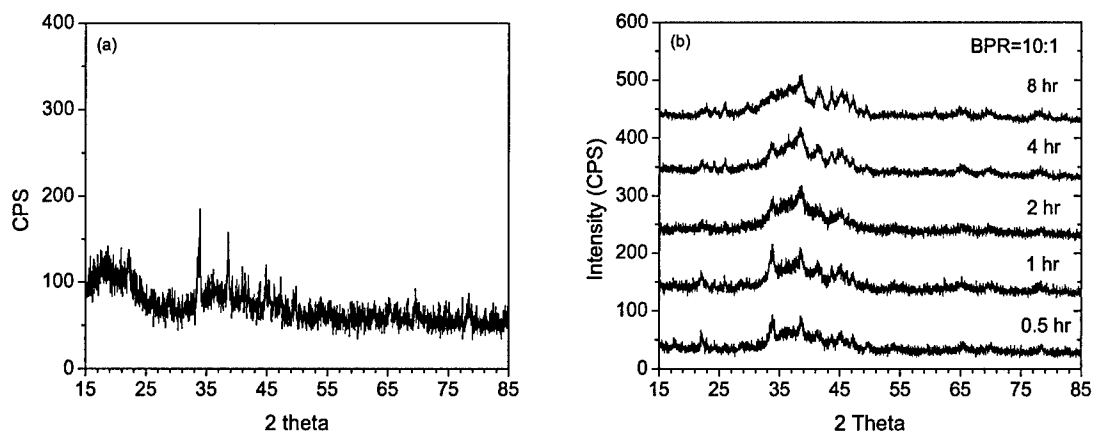(2)   A uniform distribution of nanocrystals in the amorphous matrix could be obtained.

Figure 26 XRD patterns for partially amorphous $Al_{85}Ni_{10}La_5$ ribbons: (a) before Spex milling; (b) after Spex milling.
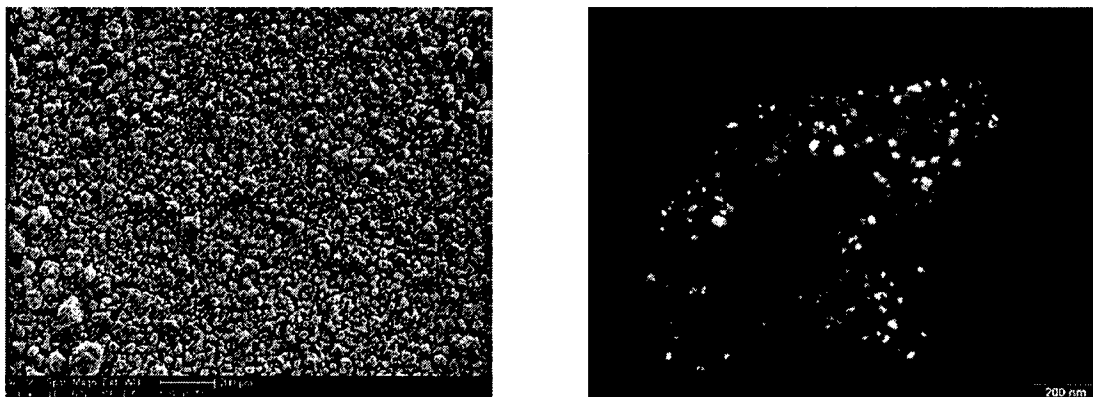

Figure 27 Morphology (a) and microstructure (b) of $Al_{85}Ni_{10}La_5$ ribbons milled for 1 hr at BPR=10

3.8 Process via Equal-Channel Angular Pressing (ECAP)

ECAP provides a unique routine for microstructure refinement and for consolidation. Processing of Fe via ECAP was investigated. The results show that:

(a) Annealed pure Fe with an initial grain size of 200 μm was processed via ECAP at room temperature. A grain size of approximately 200 nm was obtained after 8 passes (Figure 28).

(b) In tension, plastic deformation with strain softening was observed in ECAP Fe, which is different from strain hardening in annealed Fe. The ECAP-8 Fe (8 passes) still has a relatively high elongation of about 8 %. In compression of ECAP Fe, a strain-hardening region followed by a perfectly plastic deformation was observed. Intensive dislocation cell-blocks are present after one pass (Fig. 29a) and even more after subsequent pressings.

(c) The low-energy dislocation structures may have changed into the high-energy dislocation structures in the final several pressings (Fig. 29b).
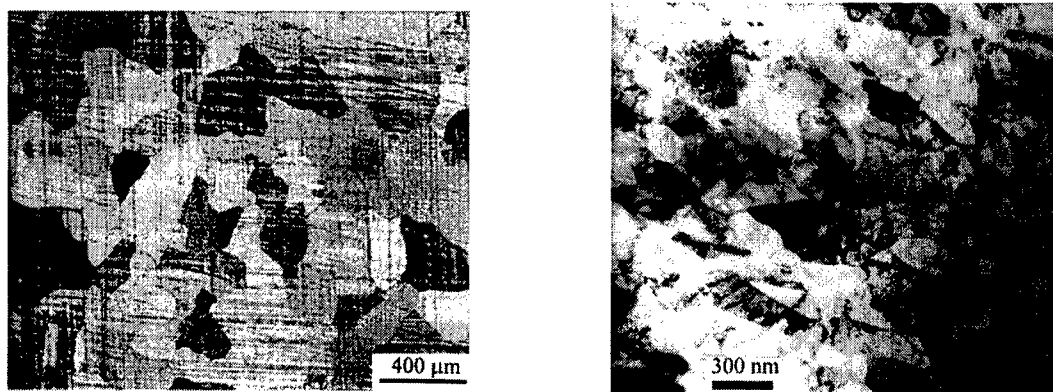

Figure 28 Microstructure of the ECAP'ed Fe in comparison with the annealed Fe: (a) The annealed Fe (Left); and (b) The ECAP'ed Fe after 8 passes (Right).
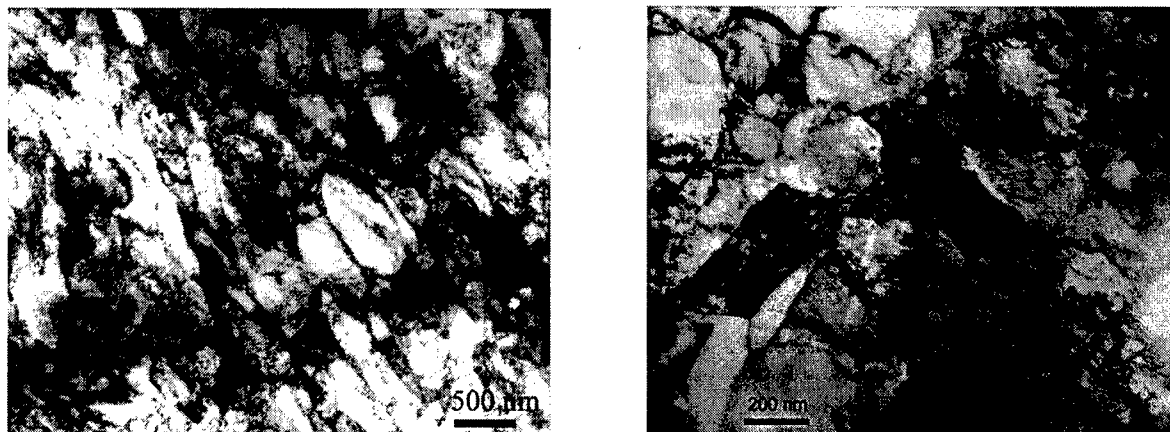

Fig. 29 (a) Dislocation-cell blocks after 1 pass and (b) Microstructure of Fe after 8 passes.

4. Suggestions for Future Study

The $Al_{85}Ni_{10}La_5$ alloy has a density of $3.53 g/cm^3$ but could own strength higher than 1000 MPa. This alloy also shows remarkably thermal stability, i.e., after consolidation an averaged grain size less than 200 nm could be achieved. Therefore, it is an interesting alloy that needs further studies in the following aspects:

    (1) To tailor the microstructure and mechanical properties of $Al_{85}Ni_{10}La_5$ /5083 Al composite by optimizing the consolidation process, as indicated in the previous part of this report, there exists large room for ductility improvement;

    (2) To study consolidation of $Al_{85}Ni_{10}La_5$ alloy via ECAP.

    (3) To study consolidation of $Al_{85}Ni_{10}La_5$ ribbons processed by cryomilling.